Sustainable Energy, Grids and Networks 38 (2024) 101332

Contents lists available at ScienceDirect

Sustainable Energy, Grids and Networks

journal homepage: www.elsevier.com/locate/segan

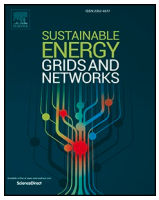

Sizing and experimental validation of a selfsync droop-based grid forming inverter with direct voltage control

Philippe Morey *, Marc Pellerin, Douglas Houmard, Mokhtar Bozorg, Mauro Carpita

School of Engineering and Management Vaud, HES-SO University of Applied Sciences and Arts Western Switzerland, Yverdon-les-Bains, Switzerland

ARTICLE INFO

Keywords:
Grid-forming inverter
Droop control
Electrical inertia
Voltage-controlled inverter
Voltage-forming inverter

ABSTRACT

Currently, the transient stability of the grid is mainly ensured by the inertial behavior of its synchronous generators. The increase of renewable energy sources connected to the grid through grid following (GFL) inverters is severely affecting the inertia of the grid and its stability is beginning to be compromised. Moreover, in case of a large disturbance, these renewable energy sources disconnect from the grid by design, thus exacerbating the problem. The idea of mimicking the behavior of synchronous generators in an inverter and participating in the grid stability gave birth to the so-called grid forming (GFM) inverters. This implies a change in paradigm from current controlled sources (GFL) to voltage-controlled sources (GFM). Despite known stability issues in current controlled converters, a typical approach to GFM converters with LCL output filters is based on cascaded current and voltage control loops. An internal current loop controls the inverter's output currents and an external voltage loop controls the filter capacitors' voltages. The problem is that this solution is complex and is also marginally stable. Alternatively, in this paper we explore a direct voltage control, which is based on droop control. The proposed control's output is used for the direct control of the inverter's output voltage in amplitude and phase. A complete analysis is performed, and a method is proposed to determine the appropriate control parameters as well as the sizing of the inverter components. Finally, an experimental setup is presented and the effectiveness of the proposed method is shown in simulations as well as in real-life experiments.

1. Introduction

With the growing proportion of renewable energy sources being connected to the grid, as well as the reduction and decommissioning of thermal (fossil or nuclear) based energy sources, stability issues begin to arise because of the proportionally reduced inertia [1]. Indeed, traditional thermal based power plants convert their mechanical power to electrical power with synchronous generators (SGs), whereas renewables, such as photovoltaic plants (PV) and wind turbines, are typically connected to the grid through grid following (GFL) inverters [2]. Unlike SGs, inverters do not intrinsically have inertia, therefore they do not participate passively in the dynamic stability of the grid. To make matters worse, in the case of severe frequency or voltage deviations caused by a large disturbance on the grid, GFL inverters are designed to disconnect, which increases the stress on the SGs. Furthermore, the GFL inverters cannot supply their loads in case of grid outage and eventually have no contribution in grid restoration following a black out. In this context, the concept of grid forming (GFM) voltage source inverters (VSI) was first conceived in the early 2000 s as a necessary building block for microgrids [2,3], even though the control of grid connected VSI had previously been studied [4]. GFM inverters not only have the advantage of being able to generate their own grid, but can also incorporate virtual inertia. Many different strategies have been proposed to generate the reference voltage amplitude and phase [5]. Probably the most obvious is the virtual synchronous machine which emulates the behavior of a SG. Much work has been done in this field (e.g., [6–11]), however emulating an SG does not take fully advantage of the freedom offered by the virtual nature of the control, as well as the opportunity to simplify the control scheme. The basic concept of virtual inertia is based on the swing equation which in essence is a second order differential equation that describes the dynamic behavior of the rotor of SGs as well as any flywheel.

Because of the low resilience of inverters to overloads, the designers of the first GFM inverters were reluctant to abandon the current control loop and instead built a voltage control loop around it (multiloop or cascaded control). However, current controlled inverters in GFL mode are known to have stability issues when the grid inductance is high [12]. Stable current controlled GFM inverters can be designed [13,14],

* Corresponding author.
E-mail address: philippe.morey@heig-vd.ch (P. Morey).

https://doi.org/10.1016/j.segan.2024.101332
Received 3 October 2023; Received in revised form 23 February 2024; Accepted 25 February 2024
Available online 27 February 2024

however they are also confronted with stability issues when the grid inductance is high. In [15] the authors show that the solution is to do direct voltage control and that the loss of direct control of the current can be effectively compensated by the implementation of a dynamic virtual impedance that kicks in when the current becomes too high. Furthermore, in [16] it is demonstrated that compared with the multi-loop droop control, direct voltage control has a simpler control structure and also provides a better dynamic performance.

Nevertheless, one could argue that GFL inverters could also help support the voltage in the case of a large disturbance on the grid. The issue is that GFL inverters depend on a phase locked loop (PLL) to follow the grid voltage. However, in the event of a short-circuit, the voltage drops to nearly zero and the PLL loses track of the phase and becomes unstable [17]. On the other hand, a system whose phase is controlled with an inertial behavior will not deviate as fast, which potentially allows it to recover directly if the disturbance is resolved rapidly (a few hundred milliseconds).

In this paper we explore a direct voltage control, which is based on the selfsync droop control [18], originally introduced in [19] and [20]. This method does not rely on a PLL to function but rather generates the reference phase of the inverter based on active power, as well as the reference voltage amplitude, based on reactive power. The voltage amplitude and phase are directly used as input to generate the pulse width modulation (PWM) controlling the power modules.

The novelty of this paper is that we propose a full methodology to adequately choose the corresponding control parameters as well as the sizing of the inverter components. In addition, we developed an experimental hardware setup to test and validate the effectiveness of the proposed methodology.

The rest of the paper is structured as follows: First, the system under study is described. Then the transfer functions that govern the behavior of the system are defined. These then allow us to analyze and propose a method to choose adequate control parameters. An experimental setup in which the proposed control is validated is then described, and results are presented. Finally, we present our future-related activities before concluding.

2. System description

Fig. 1 shows the block diagram of the droop-based control, where the amplitude of the voltage is controlled by a reactive power loop and the phase of the voltage is controlled by an active power loop.

where P_0 and Q_0 are the active and reactive power droop setpoints, $G_P(s)$ and $G_Q(s)$ are the respective droop controls, U and δ are the inverter voltage amplitude and phase, and P_{el} and Q_{el} are the electric active and reactive powers.

2.1. The selfsync control

The particularity of the selfsync control method is the feedforward on the angle, which improves greatly the stability of the system. The block diagram of the self-sync control is given in Fig. 2.

where T_m and T_e are the mechanical and electrical time constants, k_p and k_q and the respective droop coefficients, $k_p^{'}$ is a feedforward gain (detailed later), and ω_n and U_n are the nominal grid frequency and

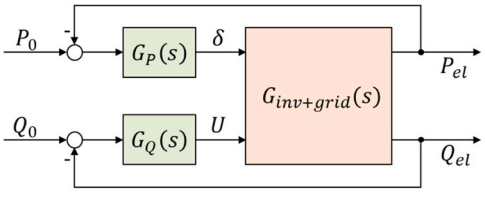

Fig. 1. Block diagram of the droop-based control of an inverter.

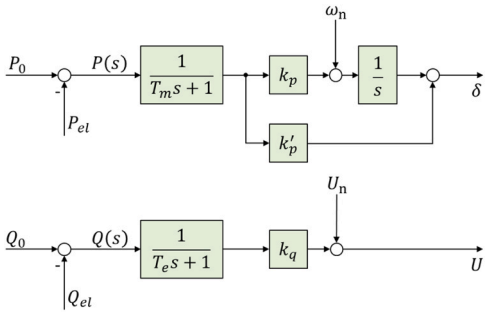

Fig. 2. Block diagram of the selfsync control as first proposed.

voltage amplitude. The corresponding transfer functions for the active and reactive power parts are:

$$G_P(s) = \frac{\delta(s)}{P(s)} = \frac{1}{T_m s+1} \cdot \left(\frac{k_p}{s} + k_p^{'}\right) \tag{1}$$

$$G_Q(s) = \frac{U(s)}{Q(s)} = \frac{k_q}{T_e s+1} \tag{2}$$

2.2. Parallel with the swing equation

The swing equation is given by Eq. (3), where M is the momentum, D is the damping coefficient, P_m is the mechanical power and P_{el} is the electrical power.

$$M\frac{d^2\delta}{dt^2} + D\frac{d\delta}{dt} = P_m - P_{el} \tag{3}$$

Applying the Laplace transform gives

$$Ms^2\delta(s) + Ds\delta(s) = P(s) \tag{4}$$

Rearranging (4) to obtain the transfer function of $\delta(s)/P(s)$ gives

$$\frac{\delta(s)}{P(s)} = \frac{1}{Ms^2+Ds} = \frac{1}{Ms+D}\cdot\frac{1}{s} \tag{5}$$

To make a parallel between the swing equation and the active power droop control, Eq. (1) can be rearranged as:

$$G_P(s) = \frac{\delta(s)}{P(s)} = \frac{1}{\frac{T_m}{k_p}s+\frac{1}{k_p}} \cdot \left(\frac{1}{s} + \frac{k_p^{'}}{k_p}\right) \tag{6}$$

Neglecting the effect of the feedforward, by identification it can be shown that the droop control emulates the behavior described by the swing equation, where the momentum (M) is equal to T_m/k_p and the damping coefficient (D) is equal to $1/k_p$. Since the damping and the droop coefficient are linked, their effects cannot be decoupled. For the ease of reading, we define a feedforward variable:

$$k_{ff} = \frac{k_p^{'}}{k_p} \tag{7}$$

Therefore, the active power droop control becomes:

$$G_P(s) = \frac{k_p}{Mk_p s+1} \cdot \left(\frac{1}{s} + k_{ff}\right) \tag{8}$$

2.3. Inertial and droop typical values

The inertia constant (H) is the ratio of kinetic energy at the nominal frequency (ω_n) to the nominal apparent power (S_N) of the generator. The order of magnitude of H is typically in the range of 1–10 seconds.

$$H = \frac{\frac{1}{2}\cdot J\cdot\omega_n^2}{S_N} \quad [s] \tag{9}$$

The momentum (M) is given by Eq. (10).

$$M = J \cdot \omega_n = 2 \cdot H \cdot \frac{S_n}{\omega_n} = \frac{T_m}{k_p} \tag{10}$$

Regarding the droop coefficients, in per units (pu)., k_p is usually 5% and k_q is 10%. The values of active power droop coefficient k_p and mechanical time constant T_m determine the value of the inertia. As for the electrical time constant T_e, it has no effect of the inertia and only defines the dynamics of the system to a voltage drop. Therefore, its value is of less importance here. However, a typical value of T_e is in the 1 second range.

3. System transfer function

3.1. Effect of the coupling with the grid

The actual inverter is equipped with an LCL filter (see Section 5). However, since the reactive power of the capacitor branch is low in comparison to the nominal power, to evaluate the coupling with the grid we neglect the capacitor branch and consider an equivalent simple RL coupling, as shown in Fig. 3. The corresponding steady-state current and voltages are shown in Fig. 4 while the equations governing the voltages and current in the rotating dq frame are given by Eq. (11).

Because it is known that the active power is strongly dependent on the phase and that the reactive power is strongly dependent on the voltage, these interactions will be referred to as "the direct influences". Furthermore, the effect of voltage on active power and phase on reactive power will be referred to as "the cross-coupling influences".

$$\begin{cases} u_{di} - u_{dg} = R \cdot i_d + L \dfrac{di_d}{dt} - \omega L i_q \\ u_{qi} - u_{qg} = R \cdot i_q + L \dfrac{di_q}{dt} + \omega L i_d \end{cases} \tag{11}$$

where u_{di} and u_{qi} are the inverter voltages, u_{dg} and u_{qg} are the grid voltages, and i_d and i_q are the currents, all in the dq axes. With these voltages and currents, the equations for active and reactive power [21]:

$$\begin{cases} P = \dfrac{3}{2}\left(u_{dg} \cdot i_d + u_{qg} \cdot i_q\right) \\ Q = \dfrac{3}{2}\left(u_{qg} \cdot i_d - u_{dg} \cdot i_q\right) \end{cases} \tag{12}$$

We define the grid voltage as being the reference, so:

$$\begin{cases} u_{dg} = \sqrt{2} \cdot U_g \\ u_{qg} = 0 \end{cases} \tag{13}$$

Furthermore, we define that the inverter voltage is offset by an angle δ, so:

$$\begin{cases} u_{di} = \sqrt{2} \cdot U_i \cdot \cos(\delta) \\ u_{qi} = \sqrt{2} \cdot U_i \cdot \sin(\delta) \end{cases} \tag{14}$$

With these two sets of equations the state-space matrixes of the multiple input multiple output (MIMO) system can be established, where the state variable $x = \begin{bmatrix} i_d & i_q \end{bmatrix}'$, input variable $u = \begin{bmatrix} \delta & U_i \end{bmatrix}'$ and the output variable $y = \begin{bmatrix} P & Q \end{bmatrix}'$.

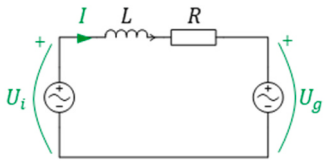

Fig. 3. Single phase equivalent schematic of the RL coupling between the inverter and the grid, where U_g and U_i are the phase to neutral grid and inverter voltages.

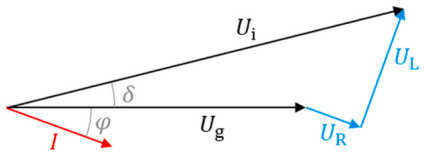

Fig. 4. Phasor diagram of the voltages and current of Fig. 3.

$$\begin{cases} \dot{x} = A \cdot x + B \cdot u \\ y = C \cdot x + D \cdot u \end{cases} \tag{15}$$

However, since the system is nonlinear, it needs to be linearized around a working point and considered for small variations. In the following section, all the variables refer to those small variations. Assuming δ is small, we linearize $\sin(\delta) \cong \delta$ and $\cos(\delta) = 1$. Furthermore, the angular velocity ω is equal to the nominal angular velocity ($\omega = \omega_n$) and the input voltage U_i is a constant, equal to the nominal voltage ($U_i = U_{ni}$). Therefore, the state-space matrixes are the following:

$$\begin{aligned} A &= \begin{bmatrix} -L/R & \omega_n \\ -\omega_n & -L/R \end{bmatrix} \qquad B = \frac{1}{L}\begin{bmatrix} 0 & 1 \\ \sqrt{2} \cdot U_{ni} & 0 \end{bmatrix} \\ C &= \frac{3}{2}\begin{bmatrix} 1 & 0 \\ 0 & -1 \end{bmatrix} \qquad D = \begin{bmatrix} 0 & 0 \\ 0 & 0 \end{bmatrix} \end{aligned} \tag{16}$$

This gives the following transfer functions for the direct influences:

$$\frac{P(s)}{\delta(s)} = U_i \cdot \frac{Q(s)}{U_i(s)} = \frac{3 U_g U_i}{X_L} \cdot \frac{\omega_n^2}{\left(s + \frac{R}{L}\right)^2 + \omega_n^2} \tag{17}$$

and for the cross-coupling influences:

$$\frac{P(s)}{U_i(s)} = -\frac{1}{U_i} \cdot \frac{Q(s)}{\delta(s)} = \frac{3 U_g}{X_L} \cdot \frac{\left(s + \frac{R}{L}\right)\omega_n}{\left(s + \frac{R}{L}\right)^2 + \omega_n^2} \tag{18}$$

Eq. (17) shows that $P(s)/\delta(s)$ and $Q(s)/U(s)$ are defined by a gain and a second order low pass filter with a resonance at ω_r, which is the constant part of the denominator.

$$\omega_{res} = \sqrt{\omega_n^2 + \left(\frac{R}{L}\right)^2} \tag{19}$$

Furthermore, this resonance is damped with a damping ratio ξ of:

$$\xi = \frac{R}{\omega_{res} L} \tag{20}$$

Eq. (18) shows that the two cross-coupling transfer functions $P(s)/U(s)$ and $Q(s)/\delta(s)$ have a lower gain than the direct influence. They have the same second order low pass behavior, with identical resonant frequencies and damping ratios, however they also have a first order high pass component. Furthermore, it is to be noted that $Q(s)/\delta(s)$ has a negative reaction, which causes the reactive power to decrease when δ increases. Fig. 5 shows the Bode diagram of the MIMO system in pu, as it is clearer in pu to evaluate the weight of each input on the outputs.

As shown, the active power is strongly linked to the phase and the reactive power is strongly linked to the amplitude of the voltage.

3.2. Sizing of the filter inductance

In steady state and neglecting the resistive component, the active power is given by Eq. (21).

$$P = \frac{3 \cdot U_g \cdot U_i \cdot \sin(\delta)}{X_L} \tag{21}$$

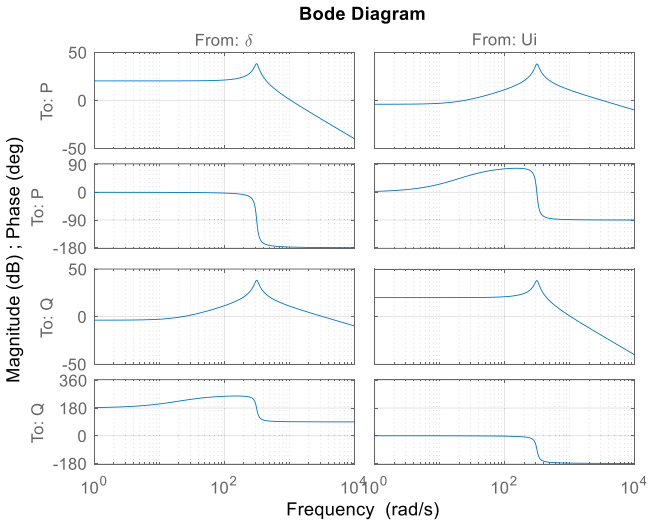

Fig. 5. Bode diagram of the MIMO system (in pu).

For the assumption of δ being small to be true, at full power the load angle has to be in the order of $\delta_{\max} \cong 0.1$ rad. This consequently implies that the single-phase inductor is:

$$L \cong \frac{3 \cdot U_n^2}{10 \cdot S_n \cdot \omega_n} \tag{22}$$

Or put otherwise, the gain (K_{inv}) of the inverter is:

$$K_{inv} = \frac{3 \cdot U_g \cdot U_i}{X_L} \cong 10 \cdot S_n \tag{23}$$

In the present case, we will consider a nominal phase to neutral voltage (U_n) of 230 V, a nominal frequency of 50 Hz $(\omega_n = 100\pi)$ and a nominal apparent power (S_n) of 10 kVA. Therefore, the single-phase inductor is $L \cong 5$ mH. This value will be retained in the design of the overall filter.

3.3. Effect of switching/sampling frequency

Assuming that the switching and sampling frequencies are the same, the delay that is induced can be modelled by a first order low pass filter.

$$G_{sampling}(s) = \frac{1}{sT_{pe} + 1} \tag{24}$$

where $T_{pe} = 3/(2f_e) + \sum_{m=1}^{n} T_m$ (f_e is switching frequency and T_m are the small time constants) [22]. Because the switching frequency is at least an order of magnitude higher that the grid frequency and that the power transfer functions have a 180° phase drop around the grid frequency, the cutoff frequencies of the active and reactive control loops will be below the grid frequency. Therefore, the effect of the switching/sampling frequency can be neglected.

3.4. Compensation of the resonant part

To avoid feedback or an excitation of the resonant part of both the active and reactive power loops, a band-stop filter is added in series in both systems (Fig. 6).

$$G_{bs}(s) = \frac{s^2 + \omega_0^2}{s^2 + \omega_1 s + \omega_0^2} \tag{25}$$

Where ω_0 is the cutoff frequency and ω_1 is the bandwidth. In the present case, $\omega_0 = \omega_1 = 100\pi$ gives satisfying results. Fig. 6 shows the new system block diagram.

Fig. 7 shows the Bode diagram of the active power inverter transfer function $G_{inv_P}(s)$, the band-stop filter, and the combination of the two.

The Bode diagram of the reactive power transfer function is the same as the one in Fig. 7, except for the gain.

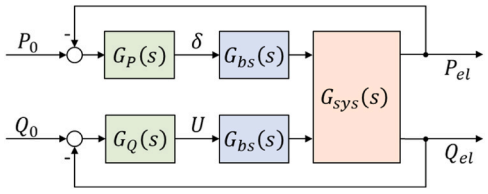

Fig. 6. Block diagram of both active and reactive droop-control chains. G_{sys} is the MIMO system described before.

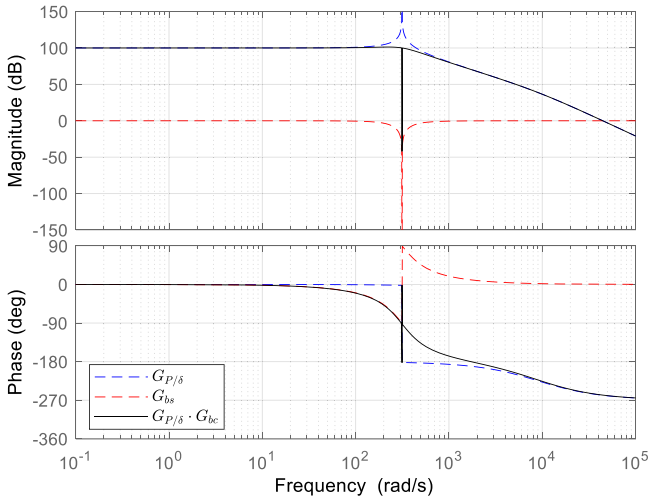

Fig. 7. Bode diagram of the active power inverter transfer function for a grid voltage of 230 V, a grid frequency of 50 Hz, a single-phase inductance of 5 mH and a switching frequency of 15 kHz.

4. Analysis and sizing of the droop control

4.1. Active power chain

The full active power chain block diagram with the droop control as developed in Eq. (6) is shown in Fig. 8.

4.1.1. System without feedforward

The first step is to analyze the system without the feedforward $(k_{ff} = 0)$. To ease the analysis, the droop control is separated into two parts:

$$G_{P_1}(s) = \frac{k_p}{Mk_p s + 1} \tag{26}$$

$$G_{P_2}(s) = \frac{1}{s} + k_{ff} = \frac{k_{ff} s + 1}{s} \tag{27}$$

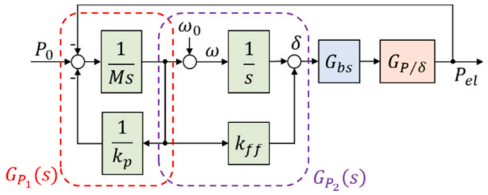

Fig. 8. Active power droop control as represented in Eq. (6) with the band stop filter and the inverter transfer functions. $G_{P/\delta}$ is $P(s)/\delta(s)$ defined in Eq. (17).

The Bode diagram of the different components of the active power droop is shown in Fig. 9.

As highlighted with the dotted line on the full system in open loop, the phase margin is close to zero, which means the system is marginally stable. The feedforward introduces a zero in the system, which is used to increase the phase margin, however as a side effect it will also decrease the attenuation of high frequencies.

4.1.2. System with feedforward

Ideally, we would like to place the zero in such a way that it does not change the cutoff frequency (ω_c) of the full system to avoid modifying the inertia. However, there is a tradeoff between the possibility of increasing the phase and not influencing the inertia. To get the most out of the zero, it should be placed close to ω_c. It can be shown that the cutoff frequency is:

$$\omega_c = \sqrt{\frac{K_{inv}}{M}} \tag{28}$$

Placing the zero at a frequency slightly lower than ω_c (20% less) allows to have a suitable phase margin (almost 60°) allowing for a dynamic response.

$$k_{ff} = 1.2\sqrt{\frac{M}{K_{inv}}} \tag{29}$$

Furthermore, to compensate for the slight shift to the right of the resulting cutoff frequency (corresponding to a lower inertia), adding k_{ff} to the denominator of G_1 gives good results (Fig. 17), without compromising the phase margin. The final proposed active power droop control is:

$$G_P(s) = \frac{k_p}{(Mk_p + k_{ff})s + 1} \cdot \left(\frac{1}{s} + k_{ff}\right) \tag{30}$$

The resulting Bode diagram is shown in Fig. 10.

The closed loop step responses for values of H ranging from 1 to 16 are shown in Fig. 11.

As shown in step responses, the response behavior is consistent when the inertia constant is varied. Furthermore, if the inverter gain (K_{inv}) is kept constant, the responses are invariable from the rated power or the nominal voltage of the inverter.

4.2. Reactive power chain

The reactive power chain shown in Fig. 2 has the disadvantage of having a static error because there is no integrator in the loop. To solve this inconvenience, we propose the diagram in Fig. 12.

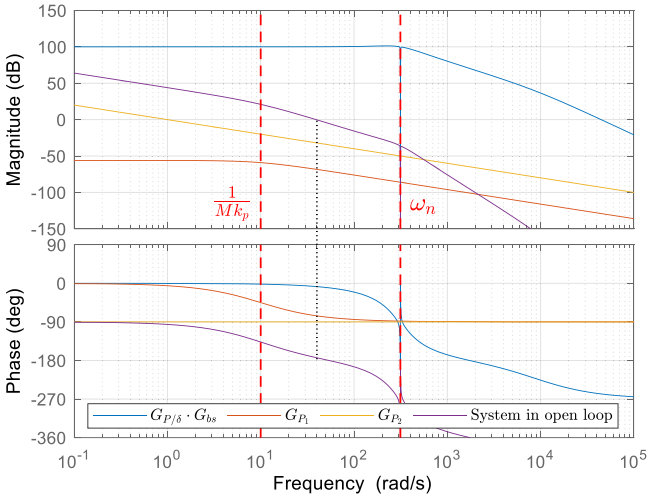

Fig. 9. Bode diagram of the different components of the active power droop control in open loop, with no feedforward. (H=1).

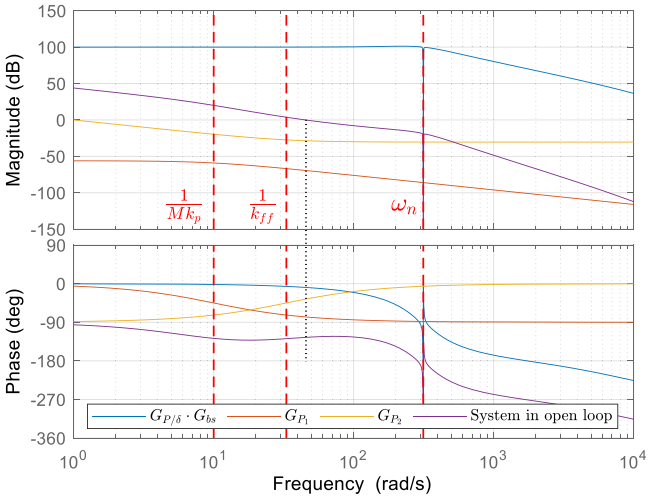

Fig. 10. Bode diagram of the different components of the active power droop control il open loop, with feedforward. (H=1).

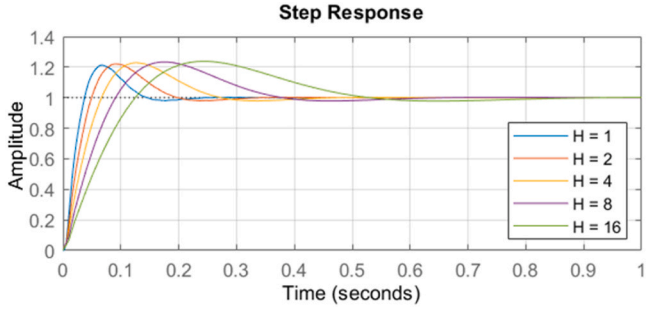

Fig. 11. Closed loop step responses of the active power droop control (in pu) for different values of H.

In the proposed control scheme, the reactive power droop is a delayed offset applied to the reactive power reference. Therefore, the tuning of the regulation is done only on the reactive power loop part as shown in Fig. 13.

The reactive power chain does not need to have high dynamics. Furthermore, since a cross-coupling exists between the active and reactive loops, slower dynamics allows for the other loop to compensate more effectively. Nevertheless, it still has to be faster than the reactive power droop time constant ($\sim \pi$ rad/s). Therefore, we choose a cutoff frequency $\omega_Q = 20$ rad/s. K_I can be calculated as the cutoff frequency divided by the steady state gain of $G_{Q/U}$.

$$K_I = \frac{\omega_Q}{K_{inv}/U_i} = \frac{\omega_Q \cdot X_L}{3 \cdot U_g} \tag{31}$$

The Bode diagram of the open loop reactive power chain as well as the different subsystems it is composed of are shown in Fig. 14.

The closed loop step response of the reactive power chain is show in Fig. 15.

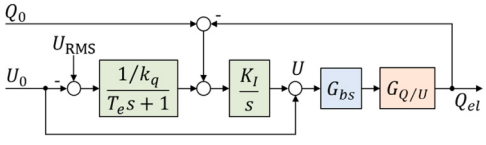

Fig. 12. Reactive power droop with the band-stop filter and inverter transfer function. $G_{Q/U}$ is $Q(s)/U(s)$ defined in Eq. (18).

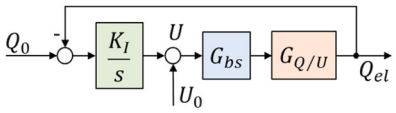

Fig. 13. Reactive power loop without the offset induced by the droop.

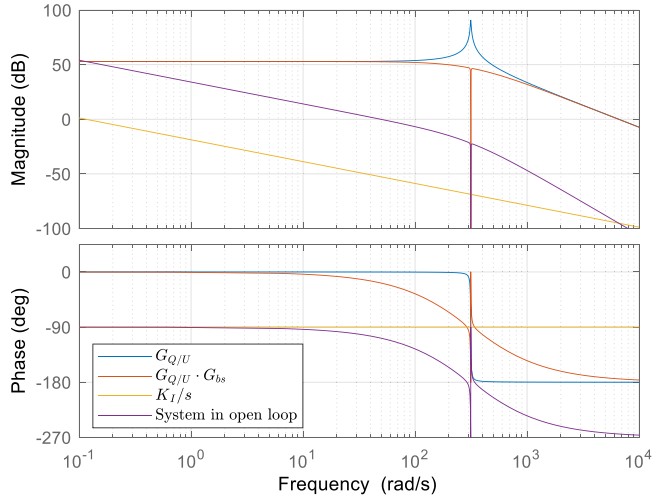

Fig. 14. Bode diagram of the different components of the reactive power chain in open loop.

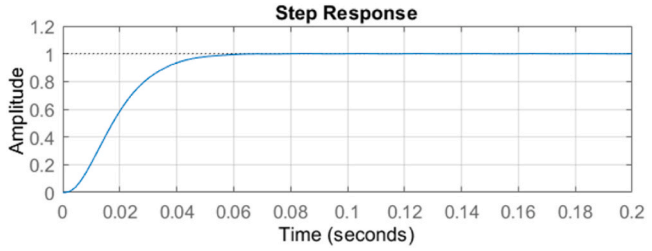

Fig. 15. Closed loop step response of the reactive power loop (in pu).

4.3. Verification with the cross-coupling effect

The system in open loop $G_{ol}(s)$ is given in (31). Applying the feedback as shown in Fig. 6

$$G_{ol}(s) = \begin{bmatrix} G_P(s) & 0 \\ 0 & G_Q(s) \end{bmatrix} \cdot \begin{bmatrix} \frac{P(s)}{\delta(s)} & \frac{P(s)}{U(s)} \\ \frac{Q(s)}{\delta(s)} & \frac{Q(s)}{U(s)} \end{bmatrix} \tag{32}$$

The system in closed loop $G_{cl}(s)$ is:

$$G_{cl}(s) = \frac{G_{ol}(s)}{1 + I \cdot G_{ol}(s)} \tag{33}$$

where I is the identity matrix. Fig. 16 shows the closed loop step response, with different inertial constants H.

As shown in Fig. 16, the cross-coupling effect is limited and is fully compensated by the regulators without any static error. Therefore, no cross-coupled compensation strategy on the active and the reactive loops have been implemented.

4.4. Simulation of the full system connected to a grid

Simulations were performed using PLECS [23]. Because the dynamics of the droop control is orders of magnitude lower than usual switching frequency and control frequency of inverters, the inverter was modeled as an ideal volage source. Furthermore, the grid was modeled as an ideal stiff grid. The simulation parameters are shown hereafter in Table 1.

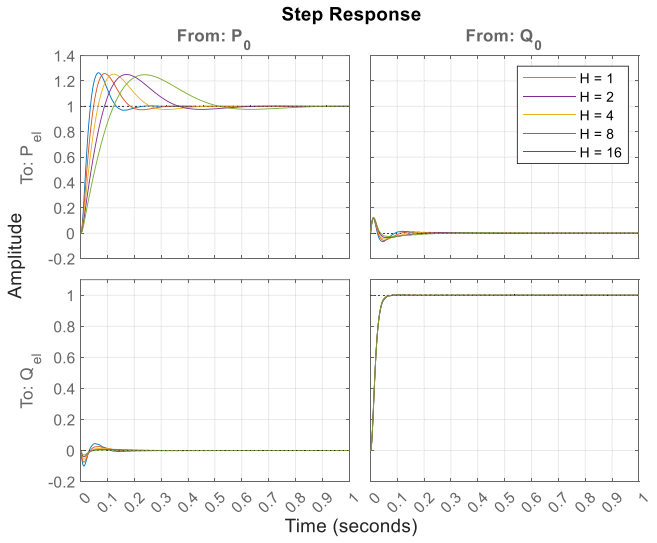

Fig. 16. Closed loop step responses with different inertial constants.

To validate the behavior of the inertial droop control, the grid frequency is varied, and the response (amplitude) is compared to the calculated ideal, non-elastic response. Fig. 17 shows the simulation result for a frequency decrease with a rate of change of frequency (ROCOF) of 1 Hz/s, with an inertia constant $H = 5$ s.

As shown in Fig. 17, the compensated response's amplitude corresponds to the ideal response and the dynamics are coherent with the ones shown in Fig. 11.

5. Experimental validation

5.1. Experimental hardware

To validate the control algorithm, a 10 kVA inverter was built and programmed in house. Fig. 18 shows the inverter in the ReIne laboratory [24] at the School of Engineering and Management (HEIG-VD) in Yverdon-les-Bains, Switzerland. This laboratory is designed to emulate different grid configurations and has a capacity up to 100 kVA.

For development purposes the inverter's DC energy source is an 800 V, 25 A, power supply. However, a high voltage battery is installed next to it is planned to replace the power supply. On the grid side, a REGATRON TC.ACS 50 kVA three phase grid simulator allows to generate the desired grid conditions, such as the frequency variations presented hereafter. The characteristics of the inverter are shown in Table 2.

To be able to provide smooth voltage when functioning in island mode, the inverter must be equipped with an LCL filter as shown in Fig. 19. Because the system is "direct voltage controlled" the variable that is controlled is the inverter voltage (labeled U_i).

Table 1
Simulation parameters.

Nominal grid voltage (L-N)	U_g	230	[V]
Nominal grid frequency	f_g	50	[Hz]
Inverter nominal power	S_N	10	[kVA]
Inverter gain	K_{inv}	100	[kVA]
Active power droop coefficient	k_p	5	[%]
Reactive power droop coefficient	k_q	10	[%]

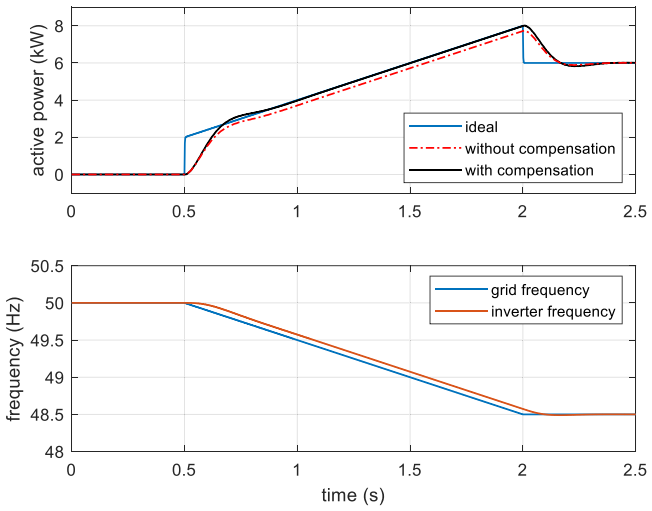

Fig. 17. Simulation result of a frequency drop with a ROCOF of 1 Hz/s and an inertia constant of H=5.

Fig. 18. The 10 kVA prototype inverter in the ReIne laboratory.

Table 2
Experimental inverter characteristics.

Nominal grid voltage (L-N)	U_g	230	[V]
Nominal grid frequency	f_g	50	[Hz]
Inverter nominal power	S_n	10	[kVA]
Inverter switching frequency	f_s	15	[kHz]
Inverter side filter inductance	L_1	3	[mH]
Filter capacitor	C	10	[μF]
Filter capacitor series resistance	R_C	3.3	[Ω]
Grid side filter inductance	L_2	4	[mH]
Active power droop coefficient	k_p	5	[%]
Reactive power droop coefficient	k_q	10	[%]

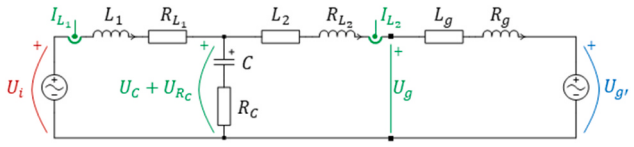

Fig. 19. Single phase schematic of the inverter to grid interface. The measured values are highlighted in green (I_{L_1},I_{L_2},$U_C + U_{R_C}$,U_g).

The phasor diagram of the currents and voltages across the LCL filter is shown in Fig. 20. Because of the absence of a PLL and the grid's phase that is not measured, the d axis is set in the inverter's reference.

Therefore, the reference voltage output by the reactive power droop is purely in the d axis and q axis is null.

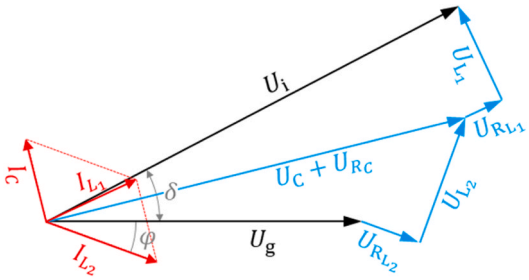

Fig. 20. Phasor diagram of the currents and voltages.

$$\begin{cases} u_{di} = \sqrt{2} \cdot U_i \\ u_{qi} = 0 \end{cases} \tag{34}$$

The main system analysis was done with an RL circuit and not an LCL. However, this is not an issue since the components of the LCL filter are known, and the different voltages and currents are measured as well. The net effect of the "L_1C" cell can be compensated by adding the voltage drop across L_1 and R_{L_1} in the dq axis to u_{di} and u_{qi}.

$$\begin{cases} u_{di} = \sqrt{2} \cdot U_i + R_{L_1} \cdot i_{d_{L_1}} - \omega L_1 \cdot i_{q_{L_1}} \\ u_{qi} = R_{L_1} \cdot i_{q_{L_1}} + \omega L_1 \cdot i_{d_{L_1}} \end{cases} \tag{35}$$

This way the circuit appears as an RL to the control algorithm.

Finally, Fig. 21 shows the complete control structure block diagram, where u_{abc_g} is a vector with the three phase measured grid voltages, $i_{abc_{L_1}}$ and $i_{abc_{L_2}}$ are respectively vectors with the three phase measured currents in L_1 and L_2, U_{DC} is the measured DC bus voltage and P_0, Q_0, U_0, and ω_0 are the reference values.

5.2. Experimental results

The inverter starts up in island mode, generating its own local microgrid, on which test loads were connected. To synchronize, a PLL is used to read the phase and amplitude of the grid voltage (while off grid). Then the synchronization with the grid is done by varying the active and reactive power references to align voltage phases and amplitudes. At the instant the inverter is connected to the grid, the active and reactive power references are returned to predefined values and the PLL is no longer used. Figs. 22 and 23 show oscilloscope screenshots (voltage and current of one phase) of step responses on the active power reference from 0 to 10 kW, with two different inertia constants ($H = 1$ s and $H = 5$ s).

The same steps were applied for values of H ranging from 1 to 16 s. The active and reactive power datapoints were measured by the inverter's microcontroller and extracted to be plotted in Fig. 24.

The measured step responses closely match the theoretical responses in Fig. 11. During the rise, a non-linearity can be observed. This is mainly due to the fact that the dead-time of the inverter switches (3μs) is significant compared to the switching period (66μs) and is not compensated. Using silicon carbide (SiC) MOSFETs would strongly reduce this effect because of the higher switching frequency capability that they offer.

Fig. 25 shows the inertial as well as the droop response of the inverter to a frequency change of 1.5 Hz, with a ROCOF of 1 Hz/s and an inertia constant $H = 5$ s.

Furthermore, the inverter has been programmed in such a way that the virtual inertia constant can be changed in real time, while the inverter is functioning, without causing any transient. This opens the possibility to explore whether and how dynamic virtual inertia can potentially improve grid stability.

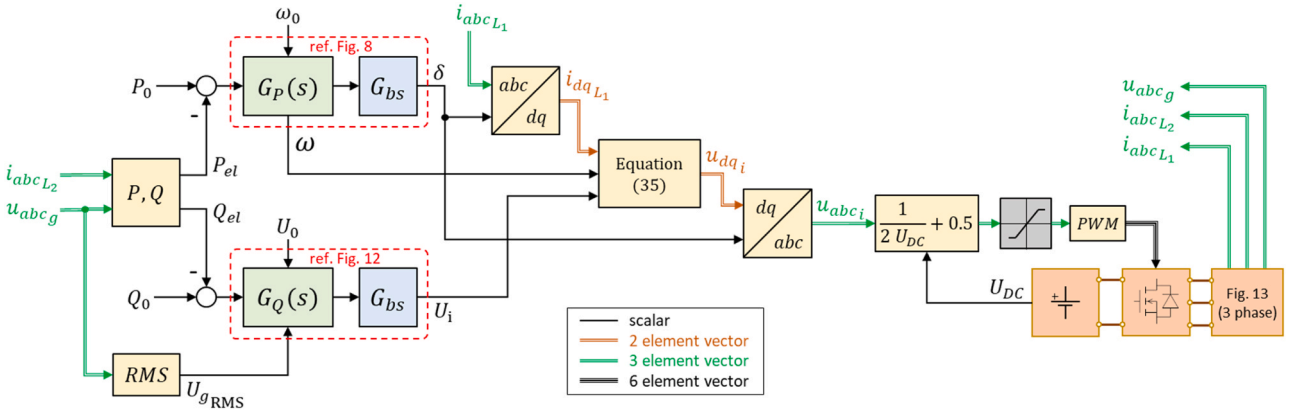

Fig. 21. Complete control structure block diagram of the implemented direct voltage control.

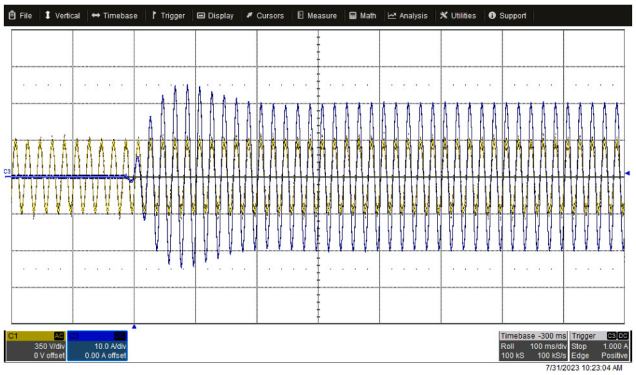

Fig. 22. Screenshot of a step response from 0 to 10 kW, for H = 1 s.

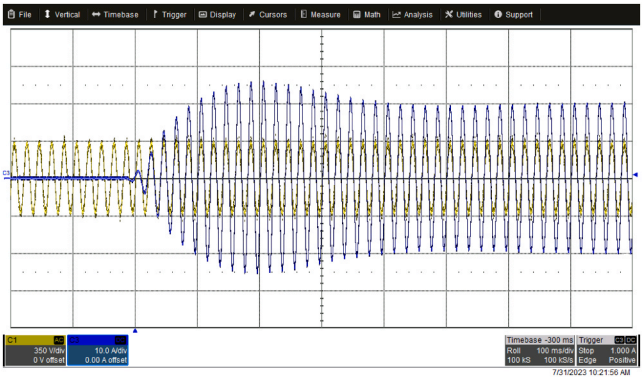

Fig. 23. Screenshot of a step response from 0 to 10 kW, for H = 5 s.

6. Limits of the proposed and tested solution

In this paper, the overcurrent protection is not explicitly addressed. On the prototype, a simple overcurrent protection has been implemented. It consists of shutting off the inverter and disconnecting it from the grid in case any measured current exceeds a predefined threshold. Nevertheless, more elaborate solutions have been studied and documented, such as in [15], where the authors propose a solution with a virtual impedance to limit the overcurrent while continuing on supporting the grid during a fault.

Furthermore, the synchronization dynamics and the associated control loops are not presented in this paper either.

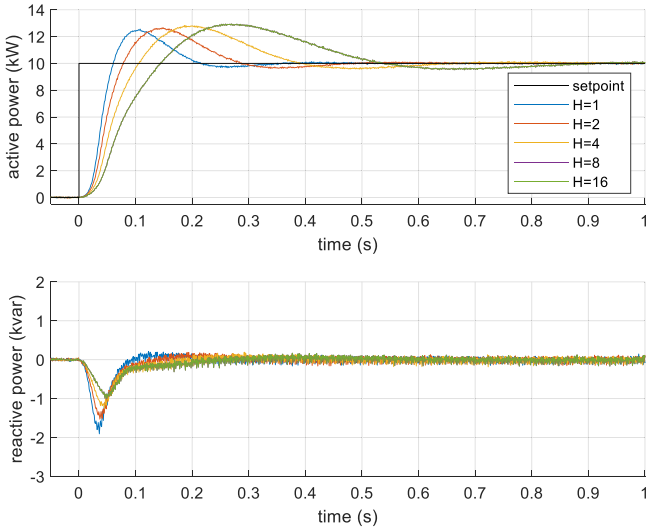

Fig. 24. Measured step responses for different inertial constants.

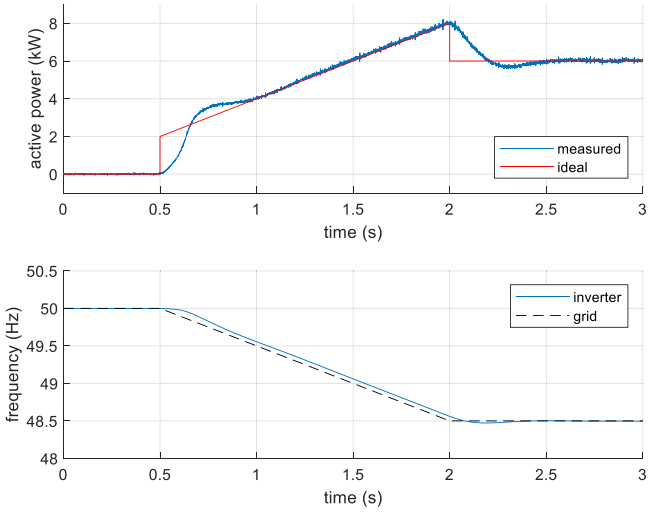

Fig. 25. Response to a change in frequency (ROCOF=1 Hz/s, H=5 s).

7. Future activities

The experimental hardware that was developed enables us to go a step further and test the real functionalities of GFM inverters as well as

their control strategies in community microgrid configurations, such as presented in [25–27]. Here we define a community microgrid as a microgrid in which several GFM inverters are installed and where their ownership is not necessarily held by a single entity. This community microgrid would be part of the macro-grid when it functions normally and would disconnect and function autonomously in case of a blackout. This allows to keep essential services running, such as water supply and treatment, as well as assist during a black start. The interactions between the GFM inverters connected to the microgrid as well as decentralized control strategies will be part of our future studies.

8. Conclusion

In this paper, we studied the selfsync droop-based control method for a GFM voltage source inverter. The reasons for using this type of control have been discussed, and a procedure for choosing and designing the various control parameters has been presented. Furthermore, the system's behavior has been simulated to showing the expected response. Following this, the algorithm has been implemented and tested on a proprietary 10 kVA inverter. The experimental results agree with the simulated ones, confirming the proposed algorithm's validity.

The next step will be to build more GFM inverters and integrate them in a community microgrid. Additionally, a high-level control layer will have to be designed to enable smart sharing of resources inside the community microgrid. Finally, this will allow us to study the interactions between the GFM inverters as well as the transition from grid connect mode to stand-alone mode.

CRediT authorship contribution statement

Philippe Morey: Formal analysis, Methodology, Software, Validation, Writing – original draft, Writing – review & editing. **Marc Pellerin:** Formal analysis, Validation, Writing – review & editing. **Douglas Houmard:** Software. **Mokhtar Bozorg:** Formal analysis, Validation, Writing – review & editing. **Mauro Carpita:** Conceptualization, Funding acquisition, Project administration, Supervision, Writing – review & editing.

Declaration of competing interest

The authors declare that they have no known competing financial interests or personal relationships that could have appeared to influence the work reported in this paper.

Data availability

Data will be made available on request.

References

[1] A. Ulbig, T.S. Borsche, G. Andersson, Impact of low rotational inertia on power system stability and operation, IFAC Proc. Vol. vol. 19 (2014) 7290–7297, https://doi.org/10.3182/20140824-6-za-1003.02615.
[2] R. Rosso, X. Wang, M. Liserre, X. Lu, S. EngelkenGrid-forming converters: an overview of control approaches and future trends ECCE 2020 - IEEE Energy Conversion Congress and Exposition , 2020, , ECCE - IEEE Energy Conversion Congress and Exposition20204292–4299, 10.1109/ECCE44975.2020.9236211.
[3] R.H. LasseterMicroGrids vol. 1 IEEE Power Engineering Society Winter Meeting. Conference Proceedings (Cat. No. 02CH37309) , 2002, , 305–308, 10.1109/PESW.2002.985003.
[4] W. Bohrer, M. Carpita, T. Ghiara, L. Puglisi, Flexible control strategy to interface solar system with privileged load and utility line, Publ by IEEE, 1989, pp. 25–30, https://doi.org/10.1109/melcon.1989.49973.
[5] U. Tamrakar, D. Shrestha, M. Maharjan, B. Bhattarai, T. Hansen, R. Tonkoski, Virtual Inertia: current Trends and Future Directions, Appl. Sci. vol. 7 (7) (2017) 654, https://doi.org/10.3390/app7070654.
[6] Y. Chen, R. Hesse, D. Turschner, H.P. BeckInvestigation of the virtual synchronous machine in the island mode in IEEE PES Innovative Smart Grid Technologies Conference Europe, 2012, 10.1109/ISGTEurope.2012.6465648.
[7] C. Li, R. Burgos, I. Cvetkovic, D. Boroyevich, L. Mili, P. RodriguezAnalysis and design of virtual synchronous machine based STATCOM controller 2014 IEEE 15th Workshop on Control and Modeling for Power Electronics, COMPEL 2014, 2014, IEEE 15th Workshop on Control and Modeling for Power Electronics, COMPEL 20141–6, 10.1109/COMPEL.2014.6877134.
[8] M. Torres, L.A.C. LopesVirtual synchronous generator control in autonomous wind-diesel power systems 1 (2009 IEEE Electr. Power Energy Conference, EPEC 2009 , 2009, IEEE Electr. Power Energy Conference, EPEC 20091–6, 10.1109/EPEC.2009.5420953.
[9] H. Wu, et al., Small-signal modeling and parameters design for virtual synchronous generators, IEEE Trans. Ind. Electr. vol. 63 (7) (2016) 4292–4303, https://doi.org/10.1109/TIE.2016.2543181.
[10] H. Bevrani, T. Ise, Y. Miura, Virtual synchronous generators: a survey and new perspectives, Int. J. Electr. Power Energy Syst. vol. 54 (2014) 244–254, https://doi.org/10.1016/j.ijepes.2013.07.009.
[11] M. Ebrahimi, S.A. Khajehoddin, M. Karimi-Ghartemani, An improved damping method for virtual synchronous machines, IEEE Trans. Sustain. Energy vol. 10 (3) (2019) 1491–1500, https://doi.org/10.1109/TSTE.2019.2902033.
[12] J. Sun, Impedance-Based Stability Criterion for, IEEE Trans on Power Apparatus Syst. vol. 26 (11) (2011) 1–10.
[13] T. Qoria, F. Gruson, F. Colas, X. Guillaud, M.S. Debry, T. PrevostTuning of cascaded controllers for robust grid-forming voltage source converter 2018 20th Power Systems Computation Conference, PSCC , 2018, Aug, , 10.23919/PSCC.2018.8443018.
[14] J.L.R. Amenedo, S.A. Gomez, J. Alonso-Martinez, M.G. De Armas, Grid-forming converters control based on the reactive power synchronization method for renewable power plants, IEEE Access vol. 9 (2021) 67989–68007, https://doi.org/10.1109/ACCESS.2021.3078078.
[15] T. Qoria, C. Li, K. Oue, F. Gruson, F. Colas, X. Guillaud, Direct AC voltage control for grid-forming inverters, J. Power Electr. vol. 20 (1) (2020) 198–211, https://doi.org/10.1007/S43236-019-00015-4/FIGURES/22.
[16] W. Du, et al., A comparative study of two widely used grid-forming droop controls on microgrid small-signal stability, IEEE J. Emerg Sel Top Power Electron vol. 8 (2) (2020) 963–975, https://doi.org/10.1109/JESTPE.2019.2942491.
[17] T. Qoria, E. Rokrok, A. Bruyere, B. François, X. Guillaud, A PLL-Free grid-forming control with decoupled functionalities for high-power transmission system applications, IEEE Access vol. 8 (2020) 197363–197378, https://doi.org/10.1109/ACCESS.2020.3034149.
[18] P. Unruh, M. Nuschke, P. Strauß, F. Welck, Overview on grid-forming inverter control methods, Energies vol. 13 (10) (2020) 2589, https://doi.org/10.3390/en13102589.
[19] A. Engler, Regelung von Batteriestromrichtern in Modularen und Erweiterbaren Inselnetzen. Ph.D. Thesis, 2001.
[20] A. Engler, Device for Parallel Operation of Equal Range Single-Phase or Three-Phase Voltage Sources., EP 1 286 444 A3, 2001.
[21] H. Akagi, E.H. Watanabe, M. Aredes, Instantaneous power theory and applications to power conditioning, Inst. Power Theory Appl. Power Conditioning (2017), https://doi.org/10.1002/9781119307181.
[22] H. Bühler, Réglage de systèmes d'électronique de puissance - Volume 1: Théorie, I., vol. I. CH-1015 Lausanne: EPFL, 2006.
[23] P.L.E.C.S. | Plexim. Accessed: Dec. 19, 2022. [Online]. Available: ⟨https://www.plexim.com/products/plecs⟩.
[24] M. Carpita, J.F. Affolter, M. Bozorg, D. Houmard, S. WasterlainReIne, a flexible laboratory for emulating and testing the Distribution grid 2019 21st European Conference on Power Electronics and Applications, EPE 2019 ECCE Europe , Sep. 2019, , 10.23919/EPE.2019.8915190.
[25] L. Che, M. Shahidehpour, A. Alabdulwahab, Y. Al-Turki, Hierarchical coordination of a community microgrid with AC and DC microgrids, IEEE Trans Smart Grid vol. 6 (6) (2015) 3042–3051, https://doi.org/10.1109/TSG.2015.2398853.
[26] B. Chen, J. Wang, X. Lu, C. Chen, S. ZhaoNetworked Microgrids for Grid Resilience, Robustness, and Efficiency: A Review IEEE Transactions on Smart Grid, vol. 12, no. 1. Institute of Electrical and Electronics Engineers Inc. , Jan. 01, 2021, , 18–32, 10.1109/TSG.2020.3010570.
[27] M.N. Alam, S. Chakrabarti, A. Ghosh, Networked microgrids: state-of-the-art and future perspectives, IEEE Trans. Industr. Inform. vol. 15 (3) (2019) 1238–1250, https://doi.org/10.1109/TII.2018.2881540.